

# Optimal Design and Physical Modelling of Mallet Percussion Instruments

Luís Henrique<sup>1</sup>, José Antunes<sup>2</sup>

<sup>1</sup>: Instituto Politécnico do Porto, Escola Superior de Música e Artes do Espectáculo IPP/ESMAE, Rua da Alegria, 4000 Porto, Portugal

<sup>2</sup>: Instituto Tecnológico e Nuclear, Applied Dynamics Laboratory ITN/ADL, Estrada Nacional 10, 2685 Sacavem, Portugal

## Summary

At the present time, instruments are mostly designed by trial and error procedures, which are inefficient and costly. In the first part of this paper we present an approach, based on finite-element eigen-analysis coupled with optimization procedures, which enable the computation of optimal instrument shapes in order to obtain a target set of modal frequencies. We briefly discuss various optimization approaches, deterministic and stochastic, in relation with computational efficiency and effectiveness. A satisfying compromise has been found by describing the shape of the vibrating components in terms of orthogonal shape-functions, and then optimizing their amplitude coefficients using a deterministic optimization scheme. Beyond enabling a systematic and cost-effective way of improving conventional instrument designs, an obvious advantage of optimization is the possibility of developing non-conventional instruments with new sound qualities. We illustrate the various aspects discussed by optimizing vibraphone or marimba-type bars, for several modal target sets. In the second part of this paper, we turn towards the sound synthesis of percussion bars. Here, the nonlinear physical modelling is based on a modal representation of the unconstrained bar. Such approach addresses the spatial aspects of the problem, being well suited for both non-dispersive and dispersive systems – which is the case of the flexural waves of interest here. Only the vibratory responses will be simulated, without an explicit accounting of sound radiation phenomena or of the coupling between vibrating bars and acoustic resonators. We illustrate the computational method with numerical simulations (sounds and animations) of marimba and vibraphone bars, for both classic and non-orthodox geometries.

**PACS no. 02.60.Pn, 05.45.-a, 43.40.Ga, 46.15. Cc**

## 1. Introduction

A significant number of modes can be excited in mallet percussion instruments. These are of paramount importance, as far as instrument intonation and timbre quality are concerned, and every effort must be provided to reach a successful design. At the present time, musical instruments are mostly designed by trial and error procedures, based on empirical knowledge and experimentation. In spite of the makers' know-how, such methods are often inefficient and costly. We think that many aspects of instrument design can be improved using a more rigorous design

approach, by coupling optimization procedures with adequate modelling techniques.

Significant developments in system modelling and optimization, during the last decades, are the result of a spectacular increase in computational hardware and software capabilities – see, for instance, [1,2]. Although mainly applied in the context of industrial problems [3,4], there have been a number of attempts to apply optimization techniques in the context of musical instruments [5-11]. Results have been in general fruitful, and efforts in this direction are still actively pursued by the authors and others [12,13]. Some aspects of

our own work in this area will be presented here, in order to elucidate how the various bar shapes used in our numerical simulations were obtained. A more detailed discussion and recent results of our work in the optimization of mallet percussion instruments will be found elsewhere [13].

In a previous paper [10], we have developed a method for the optimal design of percussion instrument bars, such as found in xylophones, marimbas and vibraphones. The aim was to compute *optimal bar shapes*, in order to comply with a pre-defined target set of modal frequencies – in other words, to shape the spectral content of the instrument response – given a number of technological constraints, which establish the acceptable ranges of the instrument physical and geometrical parameters, as well as other features such as shape simplicity.

Typically, the modal frequencies of interest will display harmonic relationships (however, one might well wish otherwise, depending on the musical context). For instance, typical values of the first and second modal frequencies for xylophones and marimbas attempt integer relationships of 1:3 and 1:4, respectively, with some variations on the third flexural modal frequency, most usually between 1:9 and 1:10. To obtain adequate intonation, the bar profile is progressively changed by trial and error, using a suitable undercut, until the target frequencies have been reached within the allowed tolerance [14].

In [10] we showed that the design of tuned bars can be greatly improved and simplified by coupling finite-element eigen-computations with a suitable optimization procedure. Indeed, for complex and innovative modal frequency relationships, such approach may prove invaluable. Values of the geometrical parameters – the bar profile  $H(x)$ , given by the height  $H_j \equiv H(x_j)$  of each mesh element – were sampled in the admissible search space. Then, for each system configuration, an eigenvalue analysis was performed using the finite-element method. A suitable error

function, to be minimized, was then computed between the eigenfrequencies obtained at each iteration and the modal target set.

Many parameters are involved in the geometry optimization problem, with two unwanted consequences: Firstly, the optimization becomes computationally intensive, and this is further true as the number of parameters to optimize  $P_p$  ( $p = 1, 2, \dots$ ) increases. Secondly, the error hyper-surface  $\mathcal{E}(P_p)$  where the global minimum is searched will display in general many local minima.

In [10] we avoided converging to sub-optimal local minima by using a robust (but greedy) global optimization technique – simulated annealing [1,2,15]. In order to improve the computational efficiency, the global optimization algorithm was coupled with a deterministic local optimization technique [1,2], to accelerate the final stage of the convergence procedure. Very encouraging results have been obtained, demonstrating the feasibility and robustness of this approach, as well as the potential to address other aspects of musical instrument design. However, a negative side effect was the need for significant computation times, which seem ill suited to the optimization of large-scale systems – such as, for instance, carillon bells.

More recently, we tried to alleviate this problem, by reducing the dimension of the search space where optimization is performed [11]. This can be achieved in several ways, by describing the geometrical profiles of the vibrating components in terms of a limited number of parameters. Here, we chose to develop  $H(x)$  in terms of a set of orthogonal shape functions  $\Psi_s(x)$ , optimizing their amplitude coefficients. For complex systems, described by finite-element meshes with hundreds or thousands of elements, this approach may reduce the size of the optimization problem by several orders of magnitude. Then, we have found that, most often, acceptable solutions can be obtained using efficient local optimization

algorithms, leading to a further reduction in computation times. Most of the examples presented in this paper have been obtained using such approach. We illustrate the various aspects discussed by optimizing vibraphone or marimba-type bars, for several modal target sets. Both classic and non-orthodox geometries are addressed.

We then turn to the physical modelling of the nonlinear responses of percussion instruments. Physical modelling of musical instruments is one of the most active areas in music acoustics, and very significant developments have been achieved in recent years [16-18]. Among these, string and wind instruments have been addressed in many significant papers. However, in spite of the relevant work offered by a few authors, idiophones – which typically display strongly dispersive waves – have received much less attention. Rossing [19] has put much effort in understanding the fascinating dynamics of many percussion instruments. Among authors interested in the physical modelling of idiophones, Chaigne and his co-workers have been particularly active in this field – see, for instance, [20-24].

Our interest in the physical modelling of impacted bars was motivated by the need to assert the timbral qualities of different designs, without the need for costly and lengthy prototype machining of each and every computed optimized bar profile  $H(x)$ . Hence, we will address here a sound synthesis problem already approached by Chaigne & Doutaut using a spatial discretisation in terms of finite differences [20]. However, we will develop a completely different approach, based on the modal representation of unconstrained bars, to address the spatial aspect of the dynamical problem. Such approach is well adapted to nonlinear problems involving both non-dispersive and dispersive systems – and, as such, suited to the flexural waves excited in idiophones, as we have shown recently [25,26].

Only the vibratory aspects will be simulated here, without an explicit accounting of the sound radiation

phenomena or of the coupling between vibrating bars and acoustic resonators – see [21,27-29]. We also assume that all nonlinear effects stem from the mallet/bar interaction, with no material or large-displacement nonlinearities – such as unmistakably found in thin-walled plates, shells, cymbals and gongs [24,30-33]. From our nonlinear numerical simulations, we have obtained bar-animations and sounds, for marimba and vibraphone bars, using both conventional and innovative designs.

## 2. Optimization procedures

We will start by briefly describing the computational approach used here to obtain the bar eigenvalues. These are needed in the error function to be minimized, and we discuss the structure of such error function. We then recall the deterministic and stochastic optimization algorithms used in the present work, as well as the relevant constraints which must apply. To conclude this section, we propose a computationally efficient approach, using orthogonal shape-functions to describe the system geometry, and develop the modified constraints which apply to such formulation.

### 4.1 Computational approach

The cross-section dimensions of bars used in marimba-like instruments are not usually small compared to their length. Indeed, as modal frequencies increase, the Bernoulli-Euler slender beam model becomes progressively inadequate. Therefore, flexural modes are here modelled in terms of the Timoshenko thick-beam model, which corrects for the effects of rotary inertia and shear deformation [34].

We will assume that only bending modes are of interest here. Obviously, for eccentric blows, torsion modes will be excited [14,35]. On the other hand, as shown by Bork et al. [35], modal displacements are three-dimensional at higher frequencies and the beam approximation becomes then clearly abusive. However, we will only

consider beam modes here, for simplicity. For the same reason, we will neglect the influence of material anisotropy and inhomogeneities, which are significant when dealing with wood bars [35,36].

Thus, for small vibratory motions, the transverse displacement  $y(x,t)$  and slope  $\phi(x,t)$  of the free conservative system are formulated as:

$$\rho A(x) \frac{\partial^2 y}{\partial t^2} + k G A(x) \left( \frac{\partial \phi}{\partial x} - \frac{\partial^2 y}{\partial x^2} \right) = 0 \quad (1)$$

$$\begin{aligned} \rho I(x) \frac{\partial^2 \phi}{\partial t^2} - E I(x) \frac{\partial^2 \phi}{\partial x^2} + \\ + k G A(x) \left( \phi - \frac{\partial y}{\partial x} \right) = 0 \end{aligned} \quad (2)$$

where the local bar cross-section area and moment of inertia are respectively  $A(x) = B H(x)$  and  $I(x) = B H(x)^3 / 12$  (with the bar width  $B$ ),  $\rho$  is the specific mass of the bar material,  $E$  is the Young modulus,  $G = 2/[2(1+\nu)]$  is the shear modulus and  $k$  is a geometric factor for the shear energy (equal to  $5/6$  for rectangular cross-sections). Inertial and stiffness terms can be easily recognized in equations (1) and (2).

Finite element discretisation of the preceding formulation leads to a linear system of equations in the classic form:

$$[\mathbf{M}]\{\ddot{\mathbf{Y}}\} + [\mathbf{K}]\{\mathbf{Y}\} = \{\mathbf{0}\} \quad (3)$$

where  $[\mathbf{M}]$  and  $[\mathbf{K}]$  are the inertia and stiffness operators, respectively (the later incorporating any boundary conditions), and  $\{\mathbf{Y}\}$  is the vector of physical displacements. In the case of bars with arbitrary height profile  $H(x)$ , we discretize the system using  $J$  elements of identical length  $l = L/J$ .

From (3), the system modal frequencies  $\omega_m$  and corresponding modeshapes  $\{\varphi_m\}$

are computed in the usual manner, assuming harmonic solutions:

$$\{\mathbf{Y}(t)\} = \{\varphi_m\} \exp(i \omega_m t) \quad (4)$$

and we obtain the classic eigenvalue formulation:

$$[[\mathbf{K}] - \omega_m^2 [\mathbf{M}]] \{\varphi_m\} = \{\mathbf{0}\} \quad (5)$$

from which the modes are computed, for each bar geometry of interest.

#### 4.2 Error function

In what follows we postulate that the material properties  $\rho$ ,  $E$  and  $G$  are known and constant. Hence, we wish to determine the optimal bar height profile  $H_j^*$  and total length  $L^*$  that lead to a given set of modal frequencies of interest  $\omega_m^{ref}$ .

Let us assume we have a bar with height profile  $H_j$  and length  $L$ , leading to the modal frequencies  $\omega_m(H_j, L)$ . An obvious term in the error function must concern deviations from the computed eigenvalues and the reference target set  $\omega_m^{ref}$ :

$$\mathcal{E}_1(H_j, L) = \left\| W_m \left[ \omega_m(H_j, L) - \omega_m^{ref} \right] \right\|_{L_r} \quad (6)$$

where  $W_m$  are weighting factors for the modal errors and  $L_r$  is a suitable norm, computed over the  $m=1, 2, \dots, M_T$  modal frequencies of the target set. Specifically, we tested the following norms:

$$L_1 = \sum_{m=1}^{M_T} |\Delta_m| ; L_2 = \sum_{m=1}^{M_T} |\Delta_m|^2 ; L_\infty = \text{MAX}_{m=1}^{M_T} |\Delta_m|$$

with  $\Delta_m = \omega_m(H_j, L) - \omega_m^{ref}$ . In most cases we did not find significant differences between results – therefore, the quadratic norm  $L_2$  is consistently used in the following illustrative computations.

To the basic error term (6), one may wish to add other terms, in order to penalize non-desirable effects, for instance excessively non-smooth (and difficult to machine) geometry profiles  $H_j$ . We did so for the optimizations presented here, by introducing an additional penalty term for the profile curvature:

$$\mathcal{E}_2(H_j, L) = \left\| \partial^2 H_j / \partial x^2 \right\|_{L_r} \quad (7)$$

so that our final error function reads:

$$\mathcal{E} = (1 - \alpha) \mathcal{E}_1(H_j, L) + \alpha \mathcal{E}_2(H_j, L) \quad (8)$$

where  $0 \leq \alpha \leq 1$  is a weighting factor of the geometrical complexity penalization – when  $\alpha = 0$  only frequency deviations are accounted; if  $\alpha = 1$  only geometrical smoothness would be of interest.

#### 4.2 Deterministic optimization

Basically, the optimization problem may be stated as finding the  $J$  element heights of  $H_j^*$  and the length  $L^*$  leading to a set of  $M_T$  modal frequencies  $\omega_m^*$  which will minimize (8). This is a problem of constrained optimization, as typically  $H_j$  and  $L$  will be limited by some admissible values, due to technological or other reasons. Then, defining a global vector  $\{\mathbf{Y}\} = \langle H_j, L \rangle^T$  of the  $J + 1$  unknowns, our optimization problem will fit the following general framework: Find the optimal solution  $\{\mathbf{Y}^*\}$  which minimises  $\mathcal{E}(\{\mathbf{Y}\})$  while complying with a set of constraints  $G_c(\{\mathbf{Y}\}) \leq 0$ , with  $(c = 1, 2, \dots, C)$ .

In our problem, the error function  $\mathcal{E}(\{\mathbf{Y}\})$  defined by (6-8) depends nonlinearly on the geometrical unknowns  $\{\mathbf{Y}\}$ , through the eigenvalue computations. However, the constraints  $G_c(\{\mathbf{Y}\})$  are here simply stated as:

$$\{\mathbf{Y}_{\min}\} \leq \{\mathbf{Y}\} \leq \{\mathbf{Y}_{\max}\} \quad (9)$$

Another common form of  $G_c(\{\mathbf{Y}\})$ , most useful in the context of §4.4, is the following matrix inequality – which generalises condition (9):

$$[\mathbf{A}]\{\mathbf{Y}\} \leq \{\mathbf{B}\} \quad (10)$$

Basically, local optimization algorithms search for a decrease in the gradient of the error function  $\nabla \mathcal{E}(\{\mathbf{Y}\})$  – that is why they are prone to being trapped in local minima. Such basic approach is inefficient, and more powerful methods rely on additional devices to improve the convergence speed. Newton and quasi-Newton schemes use (or build up) second-order local information on the error surface, and use curvature data – the local Hessian matrix – to improve convergence.

Constraints are imposed through penalty terms affecting the active constraints (using Lagrange multipliers), which force the solution to lay on the admissible workspace. The necessary conditions for optimality in a constrained problem are given by the Kuhn-Tucker equations [2,37]:

$$\begin{cases} \nabla \mathcal{E}(\{\mathbf{Y}^*\}) + \sum_c^{Active} \lambda_c^* \nabla G_c(\{\mathbf{Y}^*\}) = 0 \\ \lambda_c^* \geq 0 \end{cases} \quad (11)$$

The main equation states that, at the optimal point, the gradients of the original error function and of the active constraints (weighted by Lagrange multipliers) must cancel. Obviously, the optimality condition for unconstrained problems would be:

$$\nabla \mathcal{E}(\{\mathbf{Y}^*\}) = 0 \quad (12)$$

Many nonlinear programming algorithms have been developed to solve for the  $\lambda_c^*$  in equations (11). In the present work we used the so-called Sequential Quadratic Programming (SQP), which is an efficient quasi-Newton scheme. Further details may be found in references [2,38].

### 4.3 Stochastic optimization

Many of the available algorithms for global optimization are inspired by the ways nature works, and are based on stochastic procedures. Typical examples include genetic methods and simulated annealing (SA) [2-4]. The method used in the present work, simulated annealing, is a powerful stochastic approach originally developed by Metropolis et al. [39] as a Monte Carlo sampling technique for modelling the evolution of a solid at a given temperature. Later, Kirkpatrick et al. [40] generalized this technique, which was then applied as a global optimization procedure. We will review here briefly the main aspects of SA.

Minimizing the error function  $\mathcal{E}(\{\mathbf{Y}\})$  is seen as being analogous to the decrease of the energy state of a molten metal during cooling. At high temperature energy is high, as particles move freely everywhere. But, as temperature decreases, motions are progressively restricted and energy lowers. If the cooling schedule is sufficiently slow, particles will settle into a very ordered state, and the system will reach a global (or near-global) energy minimum. However, if cooling is enforced at a very fast rate, then particles will “freeze” in a disordered state (quenching), far from the energy minimum.

The SA analogy proceeds as a sequence of solution configurations  $\{\mathbf{Y}_i\}$ , each one randomly sampled within a certain vicinity of the last accepted iteration  $\{\mathbf{Y}_{i-1}\}$ , while a control parameter  $T$  (analogue to the cooling temperature) decreases at a sufficiently smooth rate. A very important aspect is that, when iteration moves induce an increase of the error function  $\mathcal{E}(\{\mathbf{Y}\})$ , such iterations may still be accepted – with a probability which depends on  $T$ :

$$P = \exp[-(\mathcal{E}(\{\mathbf{Y}_i\}) - \mathcal{E}(\{\mathbf{Y}_{i-1}\}))/T] \quad (13)$$

This essential feature enables the algorithm not being trapped in local minima. Additionally, the radius of the hyper-sphere centred in  $\{\mathbf{Y}_{i-1}\}$  – where the next iteration

$\{\mathbf{Y}_i\}$  will be randomly sampled – may also decrease with  $T$ .

In short: the solution space is initially explored at high “temperatures”, when many error-increasing moves are accepted, allowing the algorithm to find the region where the global minimum lays. Later, at lower “temperatures”, almost only smaller, error-decreasing moves are accepted, refining the solution.

The general SA implementation procedure is as follows:

- 1) Start from an initial “temperature”  $T_0$  and configuration  $\{\mathbf{Y}_0\}$ .
- 2) From the last accepted configuration, generate a new candidate solution  $\{\mathbf{Y}_i\}$ , randomly sampled within a certain vicinity of  $\{\mathbf{Y}_{i-1}\}$ .
- 3) Compute the error  $\mathcal{E}(\{\mathbf{Y}_i\})$  and compare with  $\mathcal{E}(\{\mathbf{Y}_{i-1}\})$ :
  - a) If  $\mathcal{E}(\{\mathbf{Y}_i\}) < \mathcal{E}(\{\mathbf{Y}_{i-1}\})$  accept the move;
  - b) If  $\mathcal{E}(\{\mathbf{Y}_i\}) > \mathcal{E}(\{\mathbf{Y}_{i-1}\})$  accept (or refuse) the move with probability  $P$  – see equation (13).  
Then go to step 2.
- 4) Repeat steps 2 and 3 for a number  $N$  of cycles. Then decrease the temperature according to a given schedule  $T_{t+1} = \mathcal{Z}(T_t)$  and continue from step 2.
- 5) When  $\mathcal{E}(\{\mathbf{Y}_i\})$  becomes less than the allowable value  $\mathcal{E}_{Tol}$ , stop the computation.

For further information on cooling strategies and other algorithm details, see for instance references [1,2,41-43].

When the global minimum “valley” has been found, convergence can be somewhat improved by coupling the global optimization algorithm with an efficient determinist approach, such as described before. As stated before, this has been done in the present computations.

#### 4.4 Shape-function approach

In order to reduce significantly the size of the optimization problem, we suggest developing the height profile in terms of a set of orthogonal functions (plus a mean value):

$$H(x) = A_0 + \sum_{s=1}^S A_s \Psi_s(x) \quad (14)$$

Obvious suitable basis functions include Fourier series and Chebyshev polynomials. Here we will illustrate the method using simple trigonometric series.

The optimisation is now performed in terms of  $S$  amplitude coefficients  $A_s$  of the shape functions, either simultaneously or in successive approximations, by progressively increasing the number of shape functions. Note that, for complex geometries, we have  $S \ll J$  and the dimension of the optimization problem may become orders of magnitude lower than using the physical mesh coordinates, as previously described. Then, the smoothness of the system shape will be mostly governed by the truncation order  $S$  of the spatial series. However, if the penalty term (7) is still used, then low-order spatial terms will be favoured in the optimization process.

We conjecture that the reduced order of the search space  $\{\mathbf{Z}\} = \langle A_s, L \rangle^T$  may lead to a “filtered” error surface  $\mathcal{E}(\{\mathbf{Z}\})$  with greater regularity than the original error function  $\mathcal{E}(\{\mathbf{Y}\})$ . Hence, if deterministic optimization strategies are attempted from scratch, they stand lower chances of being trapped in local minima. Obviously, global optimization methods can also be used to minimize  $\mathcal{E}(\{\mathbf{Z}\})$ .

Using the approach suggested here, we have to adapt the physical search-domain constraints (9) in order to accommodate the new variables  $A_s$ . This can be easily achieved using the matrix formulation (10), as follows. The original constraints are:

$$H_{\min} \leq H_j \leq H_{\max} \quad (15)$$

$$L_{\min} \leq L \leq L_{\max} \quad (16)$$

and, from (14) and (15), we obtain:

$$H_{\min} \leq \sum_{s=1}^S A_s \Psi_s(x_j) \leq H_{\max} \quad (17)$$

or, in matrix form:

$$-[\Psi]\{\mathbf{A}\} \leq -\{\mathbf{H}_{\min}\} ; [\Psi]\{\mathbf{A}\} \leq \{\mathbf{H}_{\max}\} \quad (18)$$

and, assembling conditions (16) and (18), we obtain the full matrix constraint:

$$\begin{bmatrix} -[\Psi] & \{\mathbf{0}\} \\ [\Psi] & \{\mathbf{0}\} \\ \langle \mathbf{0} \rangle & -1 \\ \langle \mathbf{0} \rangle & 1 \end{bmatrix} \left\{ \begin{matrix} \{\mathbf{A}\} \\ L \end{matrix} \right\} \leq \left\{ \begin{matrix} -\{\mathbf{H}_{\min}\} \\ \{\mathbf{H}_{\max}\} \\ -L_{\min} \\ L_{\max} \end{matrix} \right\} \quad (19)$$

### 3. Illustrative results

The previous remarks will now be illustrated on marimba-type bars. We will only address here systems symmetric with respect to their middle point. Therefore, optimization is performed only on half of the element heights  $H_j$  used in the finite element mesh, so that  $J = 32$ . Concerning the shape function approach, we used either

$$\Psi_s^C(x) = \cos(2s\pi x/L)$$

or 
$$\Psi_s^S(x) = \sin(2s\pi x/L)$$

in the first half of the bar length, with symmetry beyond. A maximum value of  $S = 10$  was used – however, for the present bar optimizations, convergence was often achieved using less orthogonal functions. In our first example we kept the bar length  $L$  as a variable to be also optimized, however it was enforced as a constant parameter in all other computations, for an easy comparison of the optimized height profiles.

The following fixed parameters were used for the modal computations:  $L = 350$  mm (when imposed),  $B = 40$  mm,  $\rho = 2840$  kg/m<sup>3</sup> and  $E = 6.726 \cdot 10^{10}$  N/m<sup>2</sup>. The valid search ranges imposed for the bar height and total length are:  $5 \leq H_j \leq 30$  mm and  $100 \leq L \leq 500$  mm (when “free”). Most of the computed bars have a fundamental

frequency of 440 Hz (except those in Figure 1, which are tuned to 880 Hz). In all the optimizations performed we used unit weight factors  $W_m$  for the modal errors. The value adopted for the penalty coefficient on the non-smoothness of  $H(x)$  was most often  $\alpha = 0.2$  (except in the examples of Figure 1, where  $\alpha = 0.3$ ).

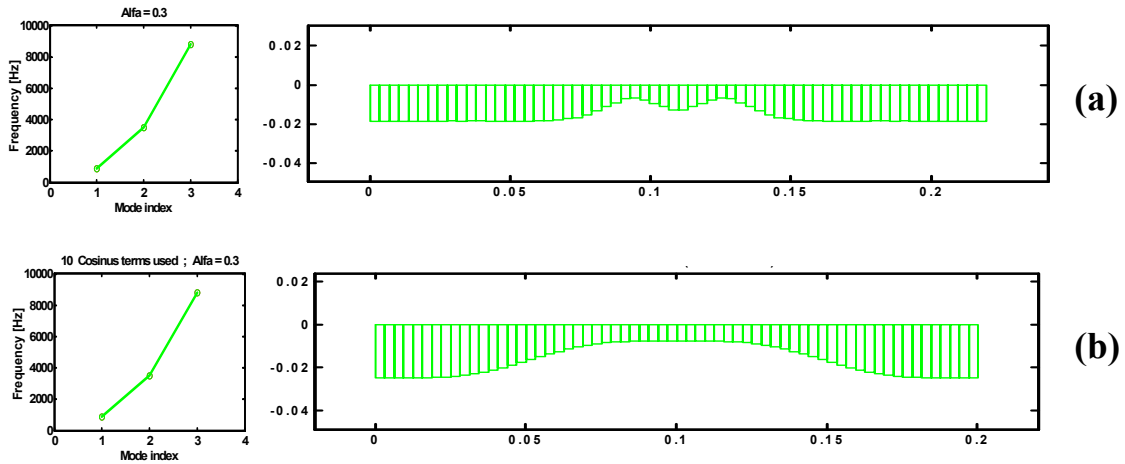


Figure 1: Optimized vibraphone bars with fundamental frequency 880 Hz and frequency relationships 1:4:10 of the tuned modes (bar length not imposed; smoothness parameter  $\alpha = 0.3$ ): (a) Stochastic optimization using SA, performed on the physical element heights; (b) Deterministic optimization using SQP, performed on the amplitudes of cosinusoidal shape-functions.

In Figure 1 we show two optimized bars with frequency relationships 1:4:10 of the tuned modes (commonly found in concert marimbas). Result (a) was obtained performing a stochastic optimization on the physical heights  $H_j$ , while result (b) pertains to a deterministic optimization performed on the shape-function amplitudes  $A_s$ . Both computed shapes are perfectly tuned for the imposed frequency relationships. However, beyond 8800 Hz, their modal frequencies will obviously be different from each other.

Notice that both optimization schemes automatically produced designs with central undercuts, as found in commercial marimba bars. Ten shape functions  $\Psi_s^C(x)$  were used for the second optimization, but three are enough to converge in such a simple problem. The important point here is that, even for this simple system, the computation time using approach (b) is typically two

orders of magnitude lower than using approach (a). Therefore, the optimization method described in §4.4 will be used in most of the following illustrations (except in Figure 3).

Figure 2 shows successive stages of the deterministic optimization approach, as the number of shape functions increases. Six terms are needed to tune five modes of a bar, on the unusual frequency relationships 1:2:4:8:16. Notice that, as the number of orthogonal functions is incremented, tuning progresses from the lower modes towards the higher modes. This is easily explained, as higher frequencies are related to shorter wave-lengths. Tuning of higher-frequency modes usually ask for the contribution of higher-order shape functions.

We have found that computations performed by optimizing simultaneously all the amplitude coefficients of the shape-function usually lead to results of comparable quality.

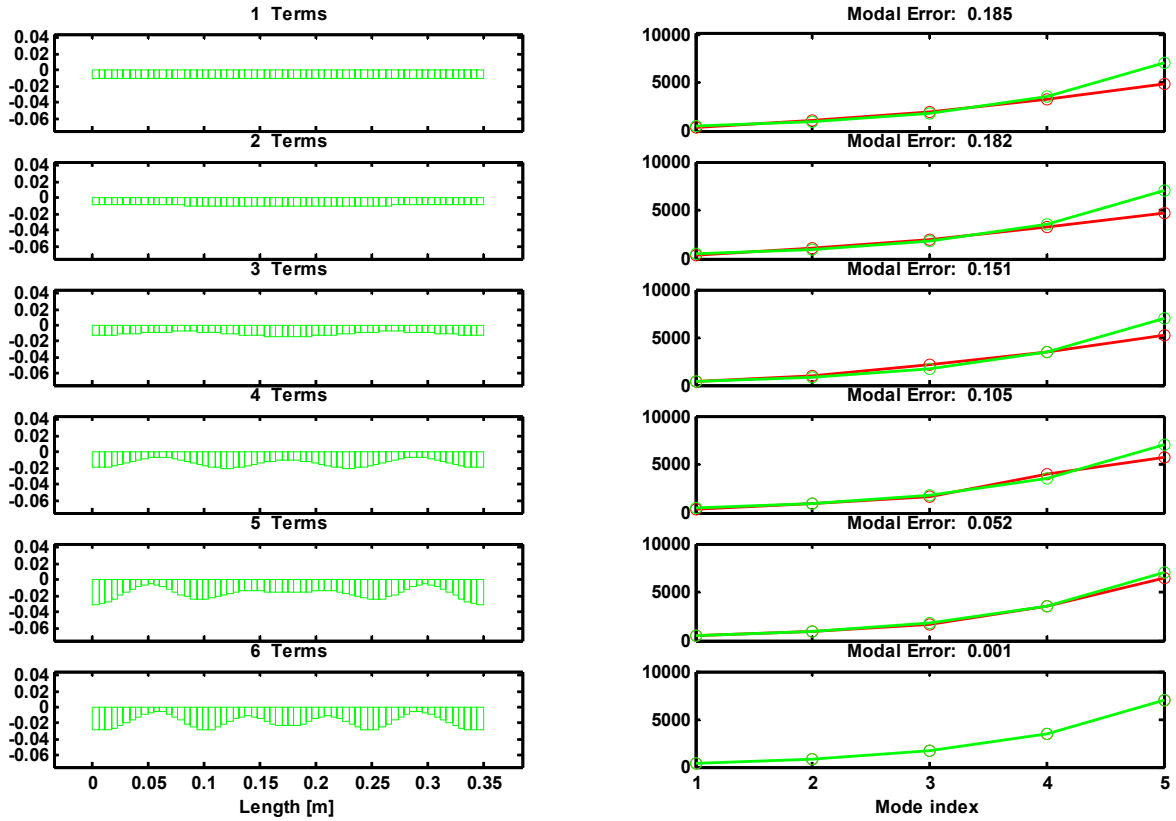


Figure 2: Deterministic optimization process of a vibraphone bar with fundamental frequency 440 Hz and frequency relationships 1:2:4:8:16 of the tuned modes (bar length imposed  $L = 0.350$  m; smoothness parameter  $\alpha = 0.2$ ): Convergence while increasing the number of shape-functions.

The influence of the smoothness parameter  $\alpha$  is shown in Figure 3. Here, stochastic optimization was performed on the geometrical variables  $H_j$ . The progressive smoothing effect, when  $\alpha$  increases, is obvious. However, if the smoothness penalty is excessively emphasised, tuning may become unfeasible – such was the case when  $\alpha = 0.8$  was imposed.

Figure 4 shows three different examples, where deterministic optimization was achieved using either  $\Psi_s^C(x)$  or  $\Psi_s^S(x)$  as shape functions. We consistently obtained adequate results, irrespective of the shape function set used. Often, both sets produced rather similar optimal shapes.

Finally, several examples of optimized bars are shown in Figure 5, corresponding to quite un-orthodox frequency relationships. This illustrates the power of an optimization approach to generate new instruments, when suitable design criteria can be established.

## 4. Nonlinear dynamical modelling

The computational method used here is described next:

(1) From the optimized bar profile  $H(x)$  and the physical properties of the bar, we compute the planar flexural vibration modes of the unconstrained system in the audible frequency range. At this stage, as in Section 2, we use the finite-element method with computations based on the Timoshenko beam model. The boundary conditions used are those of a free-free bar, which imply the existence of two rigid-body zero-frequency planar modes (translation and rotation), as well as the modes with elastic deformation. Again, as in Section 2, we will ignore here for simplicity the torsion modes and high-frequency 3-D effects. However, the use of a more accurate modal basis, computed from an extensive 3-D mesh of massive elements, would not change in any way the numerical approach used here for the time-

domain simulations. Indeed, the use of modes based on such a refined model would further highlight the computational efficiency of the modal approach, when compared for instance with time-domain finite-element computations.

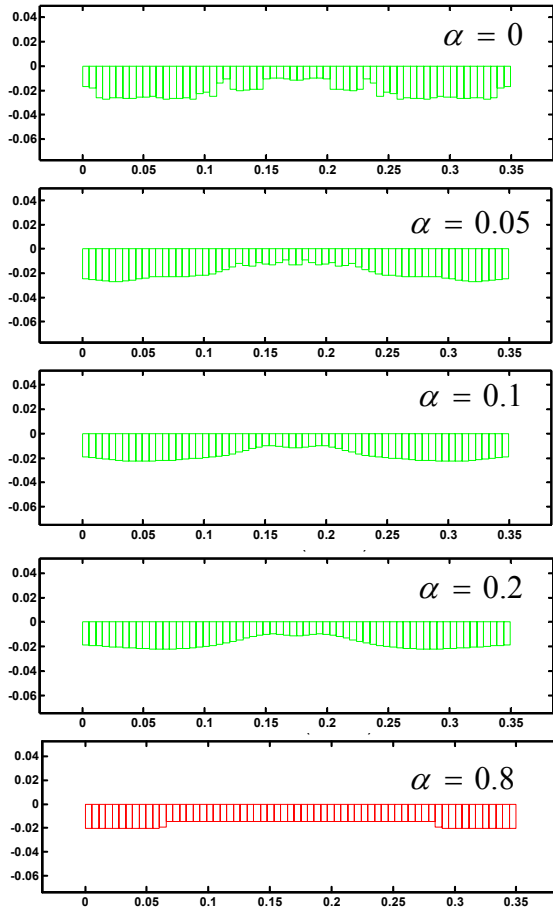


Figure 3: Stochastic optimization of a vibraphone bar with fundamental frequency 440 Hz and frequency relationships 1:4:10 (bar length imposed  $L = 0.350$  m): Results as a function of the smoothness parameter  $\alpha$ .

(2) When performing the dynamical computations, the modal damping values used clearly affect the bar dynamics, as well as the subjective perception of the simulated sounds. Due to the nature of the various dissipative phenomena, damping values are usually frequency-dependent, as discussed in [22,23,36,44,45]. Although this is a subtle aspect, we used – again for simplicity – constant values for all modes in our

computations. Note, however, that the modal model can accommodate most easily any frequency-dependency of the damping coefficients. The average values used in the present computations were based on experimental identifications. Obviously, these values are very different for wood and for aluminium bars.

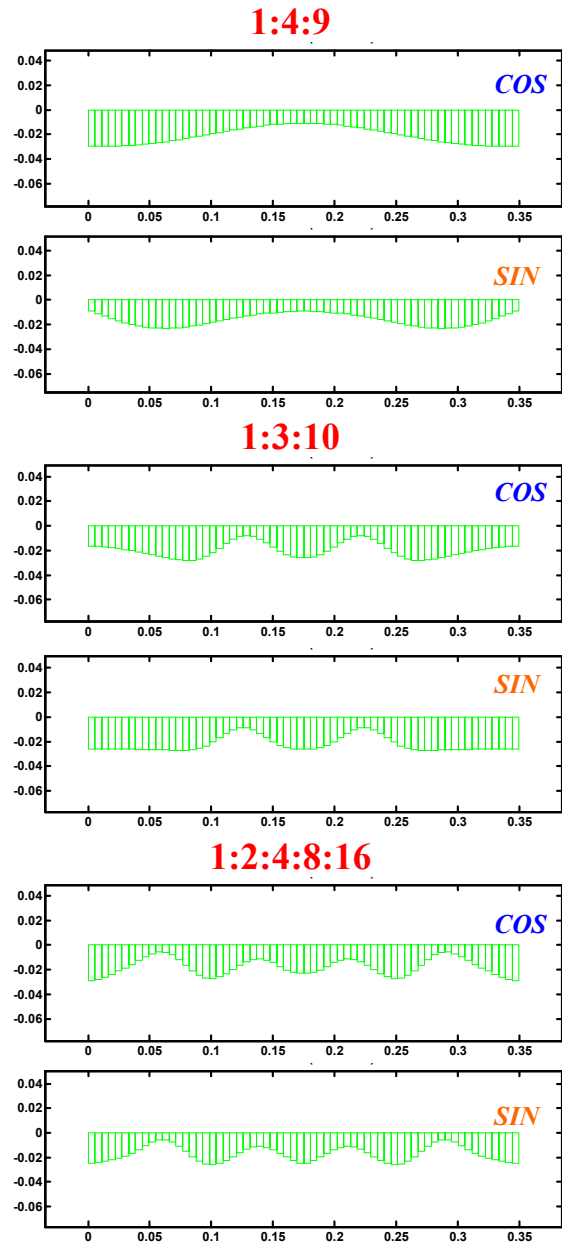


Figure 4: Deterministic optimization of three vibraphone bars with fundamental frequency 440 Hz (bar length imposed  $L = 0.350$  m; smoothness parameter  $\alpha = 0.2$ ): Results using 10 cosinusoidal or sinusoidal shape-functions.

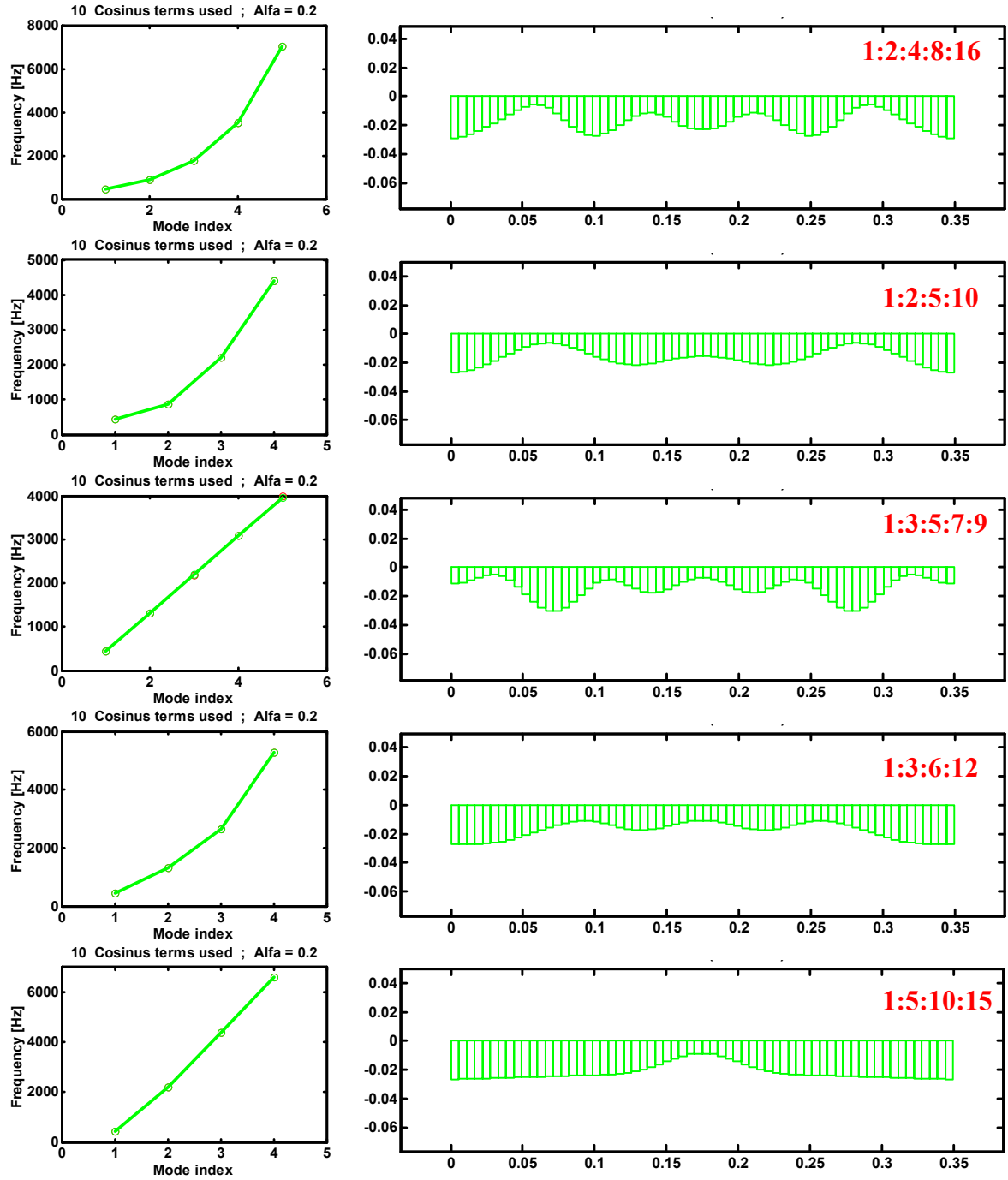


Figure 5: Deterministic optimization of several non-orthodox vibraphone bars with fundamental frequency 440 Hz (bar length imposed  $L = 0.350$  m; smoothness parameter  $\alpha = 0.2$ ).

(3) The vibrating bars are assumed supported at two locations  $x_{s1}$  and  $x_{s2}$  through flexible dissipative fixtures. The stiffness constant  $K_s$  and damping constant  $C_s$  used in the computations are based on experimental results.

(4) We assume that the bar is impacted by a point mass  $M_c$  with initial velocity  $V_c$  at the nominal contact location  $x_c$ . As other authors, we will use a simple Hertz model, to relate the nonlinear contact force (at the nominal contact point) to the relative bar/mallet motion after impact [20]. This

interaction point-model is a very convenient approximation. A more accurate contact model might be easily implemented in our computations, by including the elastic modes of the mallet as well as by using a time-dependent contact length, as a function of the mallet geometry and of the bar/mallet elastic interpenetration. Also, dissipative contact phenomena could easily be incorporated in the model. However, if the parameters used in Hertz-type models are well chosen, quite realistic results can be obtained even with this simple contact model. The mallet physical parameters (inertia and stiffness) and the impact velocity used in our computations are based in experimental data by Bork [46].

(5) At each time-step  $n$ , we compute by modal superposition the physical vibratory responses at locations  $x_{s1}$ ,  $x_{s2}$  and  $x_c$ . This enables the computation of the interaction forces between the bar and the two elastic supports,  $F_{s1}(t)$  and  $F_{s2}(t)$ , as well as the contact force between the bar and the mallet,  $F_c(t)$ . These interaction forces are then projected on the modal basis, and the dynamic modal equations are integrated one step ahead using an explicit algorithm. This scheme is pursued for the full duration  $T$  of the simulation.

#### 4.1 Bar dynamics

We will now formulate the equations used in our computational scheme. Let us then consider a bar of length  $L$ , constant width  $B$  and variable height profile  $H(x)$ . In terms of the chosen modal representation, the system dynamics are governed by:

$$[\mathcal{M}]\{\ddot{Q}\} + [\mathcal{C}]\{\dot{Q}\} + [\mathcal{K}]\{Q\} = \{\mathcal{F}\} \quad (20)$$

Here the modal matrixes are given as:

$$\begin{cases} [\mathcal{M}] = \text{Diag}(\mathbf{m}_1, \mathbf{m}_2, \dots, \mathbf{m}_M) \\ [\mathcal{C}] = \text{Diag}(\mathbf{c}_1, \mathbf{c}_2, \dots, \mathbf{c}_M) \\ [\mathcal{K}] = \text{Diag}(\mathbf{k}_1, \mathbf{k}_2, \dots, \mathbf{k}_M) \end{cases} \quad (21)$$

with:

$$\begin{cases} \mathbf{m}_m = \int_0^L m(x) [\varphi_m(x)]^2 dx \\ \mathbf{c}_m = 2\mathbf{m}_m \omega_m \zeta_m \quad ; \quad \mathbf{k}_m = \mathbf{m}_m \omega_m^2 \end{cases} \quad (22)$$

where  $\omega_m$  and  $\zeta_m$  stand, obviously, for the modal (circular) frequencies and damping values, and  $\varphi_m(x)$  are the bar modeshapes. The modal masses depend on the modeshapes, as well as on the bar profile through the mass per unit length  $m(x) = \rho A(x) = \rho B H(x)$ . As stated before, for each bar geometry, all modal parameters are computed, once and for all, using a finite-element model based on equations (1) and (2).

The vectors of modal responses and modal forces are given as:

$$\begin{cases} \{Q\} = \langle q_1(t), q_2(t), \dots, q_M(t) \rangle \\ \{\mathcal{F}\} = \langle \mathbf{f}_1(t), \mathbf{f}_2(t), \dots, \mathbf{f}_M(t) \rangle \end{cases} \quad (23)$$

and, at any location  $x$ , the physical response  $y(x, t)$  can be simply computed from the modal amplitudes  $q_m(t)$  through modal superposition:

$$y(x, t) = \sum_{m=1}^M \varphi_m(x) q_m(t) \quad (24)$$

and similarly concerning the velocities and accelerations.

The modal forces are obtained through modal projection of all the external forces. For this system, these are the two support reactions and the mallet/bar interaction force. Hence:

$$\begin{aligned} \mathbf{f}_m(t) &= \int_0^L \begin{bmatrix} F_{s1}(t) \delta(x - x_{s1}) + \\ F_{s2}(t) \delta(x - x_{s2}) + \\ F_c(t) \delta(x - x_c) \end{bmatrix} \varphi_m(x) dx \\ &= F_{s1}(t) \varphi_m(x_{s1}) + \\ &\quad F_{s2}(t) \varphi_m(x_{s2}) + \\ &\quad F_c(t) \varphi_m(x_c) \end{aligned} \quad (25)$$

where  $\delta(x)$  is the Dirac distribution.

## 4.2 Mallet dynamics

In our model, the mallet is modelled simply as a point mass  $M_c$  with initial velocity  $V_c$ , interacting with the bar at location  $x_c$ . If  $z(t)$  is the motion of the impactor, then the mallet dynamics will be governed by:

$$M_c \ddot{z} = F_c(t) - M_c g \quad (26)$$

where  $g$  is the acceleration due to gravity.

## 4.3 Impact force

The Hertz model used here leads to the following contact force:

$$F_c(t) = \begin{cases} 0 & \text{if } z(t) - y_c(t) \geq 0 \\ -K_c [z(t) - y_c(t)]^s & \text{if } z(t) - y_c(t) < 0 \end{cases} \quad (27)$$

where  $y_c(t) \equiv y(x_c, t)$  and  $s = 3/2$ . Note that equation (25) insures that only modes such that  $|\varphi_m(x_c)| \neq 0$  will be excited by the mallet.

## 4.4 Support forces

The bar supports, modelled as linear flexible-dissipative fixtures, lead to the following reaction forces:

$$F_{sj}(t) = -K_s y_{sj}(t) - C_s \dot{y}_{sj}(t) ; j=1,2 \quad (28)$$

where  $y_{sj}(t) \equiv y(x_{sj}, t)$ . Again from equation (25), we note that only modes such that  $|\varphi_m(x_{sj})| \neq 0$  will be affected by the supports. If – as is usual practice – the supporting fixtures are located at the nodes of the first mode, then only higher-order modes will suffer additional damping from the supports.

## 4.5 Time-step integration

There are many integration algorithms that might be used to integrate equations

(20) – Runge-Kutta, Verlet, among others. We used the Euler-Richardson scheme, which is of the explicit type [1]. In this algorithm, an estimate of the acceleration vector is performed at the next half-step  $t_{n+1/2} \equiv t_n + \Delta t/2$ , using the information at time  $t_n$ :

$$\left\{ \begin{array}{l} \left\{ \dot{Q}_n \right\} + \left\{ \ddot{Q}_n \right\} \frac{\Delta t}{2}, \\ \left\{ \ddot{Q}_{n+1/2} \right\} = [\mathcal{M}]^{-1} \left\{ \mathcal{F} \left\{ \dot{Q}_n \right\} + \left\{ \ddot{Q}_n \right\} \frac{\Delta t}{2}, \right. \\ \left. t_n + \frac{\Delta t}{2} \right\} \end{array} \right\} \quad (29)$$

which is then used to update displacements and velocities at time  $t_{n+1}$ :

$$\left\{ Q_{n+1} \right\} = \left\{ Q_n \right\} + \left( \left\{ \dot{Q}_n \right\} + \left\{ \ddot{Q}_{n+1/2} \right\} \frac{\Delta t}{2} \right) \Delta t \quad (30)$$

$$\left\{ \dot{Q}_{n+1} \right\} = \left\{ \dot{Q}_n \right\} + \left\{ \ddot{Q}_{n+1/2} \right\} \Delta t \quad (31)$$

## 5. Numerical simulations

We will present now some sample computations, using several optimized bar geometries computed as shown in Sections 2 and 3. Apart from the “static” plots presented here, we also have generated animations of the bar responses and the corresponding sound files. Parametric computations have been performed, to illustrate the influence of:

- the impact location  $x_c$ ;
- the bar material;
- the mallet stiffness;
- the bar modal frequency ratios.

Parameters kept constant in our computations are the mallet mass  $M_c = 20$  g and impact velocity  $V_c = 1$  m/s, as well as the support stiffness  $K_s = 10^4$  N/m and dissipation  $C_s = 20$  Ns/m. For all the geometries computed we postulated that supports are located at the nodes of the first

elastic mode of the unconstrained bar. The first modal frequency is 440 Hz, for all the computed bars, irrespectively of their shape or material. As stated before, besides the first tuned modes of the optimized bars, all modes in the range  $0 \sim 20$  kHz were used in the numerical simulations.

The numerical simulations presented here extend for 5 seconds – which is enough

to highlight both the initial transient and the subsequent decay. Sound files have been generated at the usual sampling rate of  $f_s = 44.1$  kHz. Computational speed was not an important issue for the numerical simulations presented here, therefore a very comfortable time-step of  $\Delta t = 2.3 \cdot 10^{-6}$  s was used.

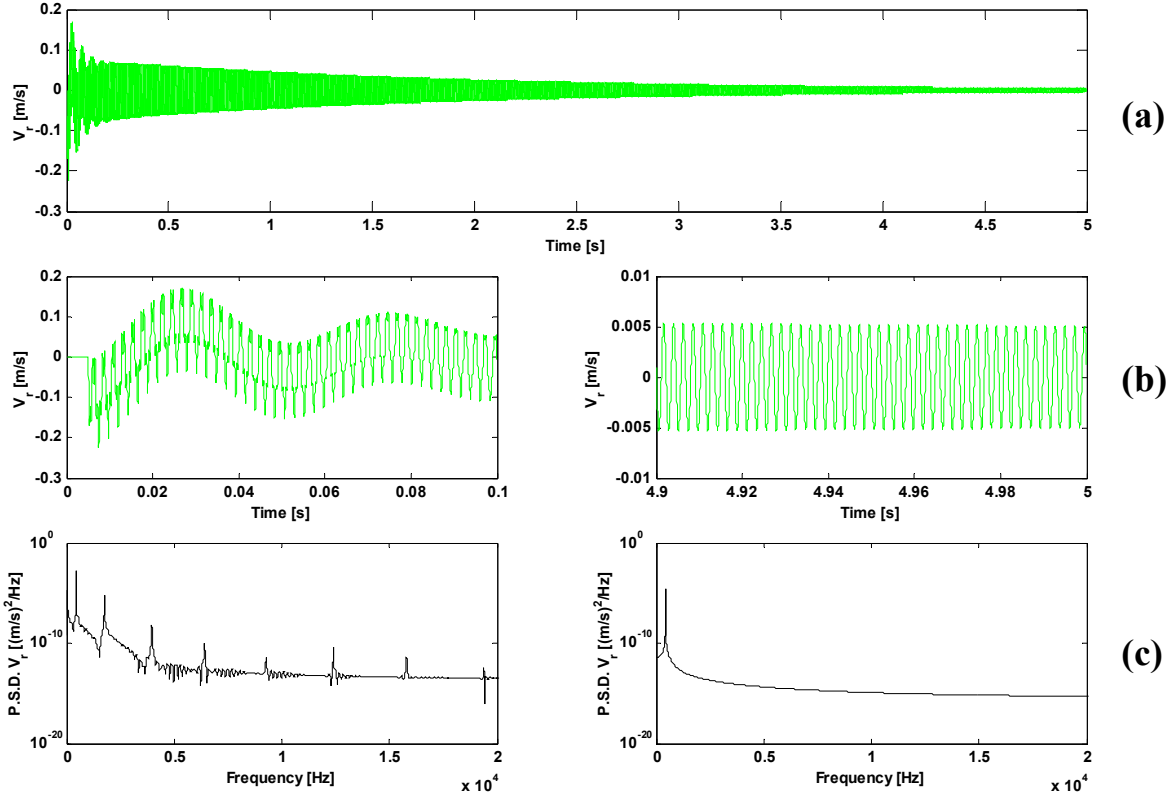


Figure 6: Typical response of a 1:4:9 vibraphone bar impacted at location  $x_c = 0$  using a mallet with contact stiffness  $K_c = 10^8$  N/m<sup>3/2</sup>: (a) Time-history of the velocity response at the bar end  $x = 0$ ; (b) Detail of the velocity response during the initial transient and the final decay; (c) Velocity spectra during the initial transient and the final decay.

## 5.1 Results

As a first example, Figure 6 (a-c) shows several aspects of the vibratory response of a vibraphone bar, when impacted at location  $x_c = 0$ . For this aluminium bar, which has a typical undercut, we postulated modal frequency ratios of 1:4:9 for the tuned modes. A modal damping value of  $\zeta_m = 0.02\%$  has been assumed for all modes, as explained before. A contact

stiffness value of  $K_c = 10^8$  N/m<sup>3/2</sup> between the mallet tip and the bar – see equation (27) – has been used.

The time history trace in Figure 6 (a) shows the initial transient after the mallet impact, followed by the slow decay of the first elastic mode. The first zoomed trace in Figure 6 (b) highlights how, during the initial transient, the low-frequency support-dependent rigid-body modes are excited, as

well as the higher frequency elastic modes. The second zoomed trace shows that the decay response is dominated by the lightly damped first elastic mode. These effects are confirmed by the corresponding response spectra shown in Figure 6 (c).

The spectrogram of the bar response at location  $x_c = 0$  is illustrated in Figure 7. It is clear that the higher frequency modes only vibrate significantly during a few tenths of a second – which are however crucial for the timbre recognition. Overall, we feel that the perceived “sound” (we used

the velocity signal at a bar end for our subjective timbre comparisons) is quite realistic, although the resonator has not been incorporated yet in the model.

In Figure 8 we display the relative energies of the system modes (notice that the energy scale is logarithmic). Clearly, most of the impact energy goes to the first elastic mode – number 3 in this plot. The two low frequency rigid-body modes also vibrate significantly. The energy of the higher frequency elastic modes decreases fast, as the modal frequency increases.

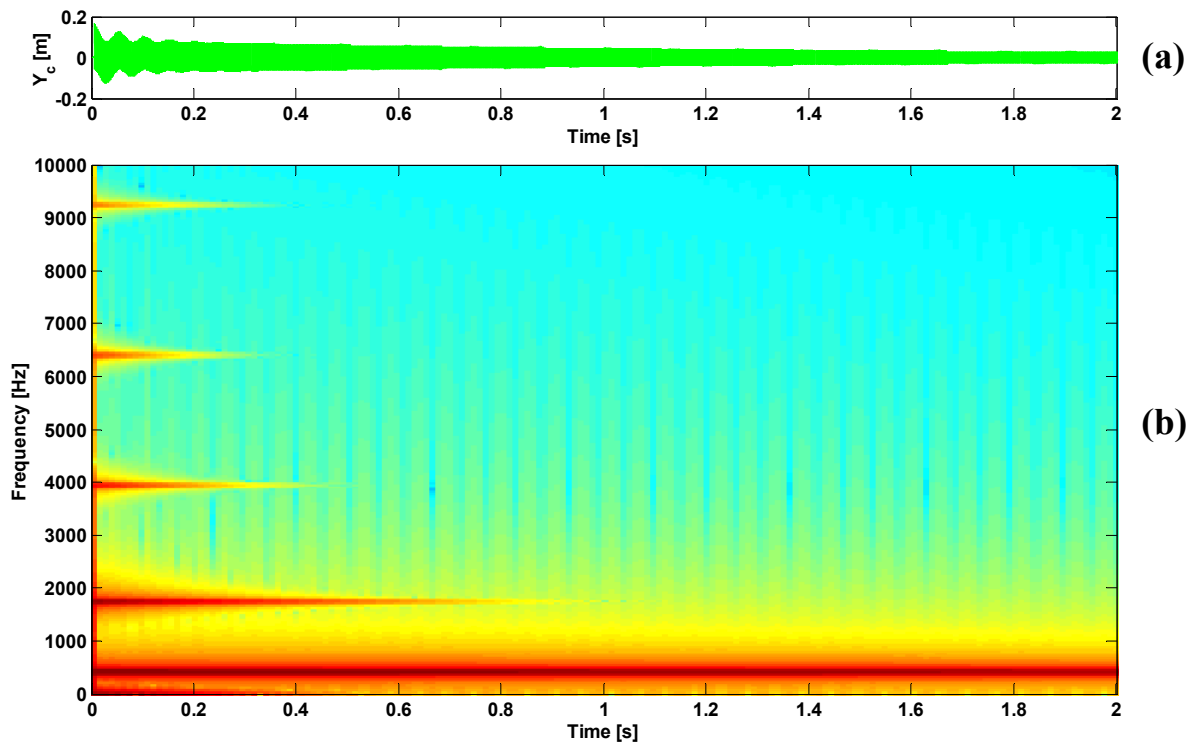


Figure 7: Typical response of a 1:4:9 vibraphone bar impacted at the bar end  $x_c = 0$  using a mallet with contact stiffness  $K_c = 10^8 \text{ N/m}^{3/2}$ : (a) Time-history of the velocity response at the impact location; (b) Corresponding spectrogram.

## 5.2 Impact location

We will now discuss, through parametric computations, several aspects which are particularly significant for the vibratory responses of this system. Figure 9 shows the time-responses and corresponding spectrograms of the same 1:4:9 vibraphone bar, as a function of the impact

location  $x_c$ , when a mallet with contact stiffness  $K_c = 10^8 \text{ N/m}^{3/2}$  is used. The corresponding sound files show clear differences in the perceived sounds. The sounds obtained at  $x_c = L/10$  and  $x_c = L/3$  are rich and well balanced (the typical “vibraphone-sound” one usually

hears). However, because the nodes of the fundamental mode are located near  $x_c = L/5$ , striking the bar near the supports will induce a “thin” sound, rich at higher frequencies but poor as far as the

fundamental is concerned. On the other hand, when the mallet strikes the middle of the bar, only the symmetric modes are excited. The corresponding sound is comparatively dull.

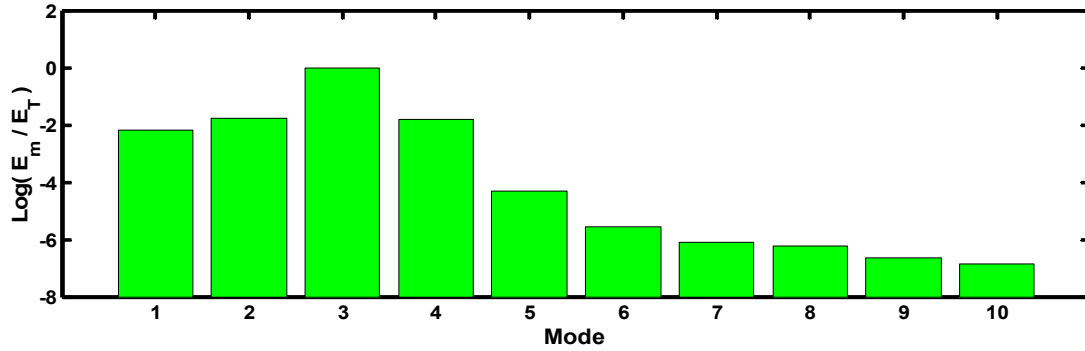


Figure 8: Typical response of a 1:4:9 vibraphone bar impacted at location  $x_c = 0$  using a mallet with contact stiffness  $K_c = 10^8 \text{ N/m}^{3/2}$ : Relative modal energies.

### 5.3 Contact stiffness

Figure 10 shows the time-responses and corresponding spectrograms of the same 1:4:9 vibraphone bar, as a function of the contact stiffness  $K_c$ , when the mallet strikes at location  $x_c = L/10$  (the influence of the bar material is also shown here and will be discussed in next). The extreme values of the contact stiffness used in these simulations,  $10^7$  and  $10^9 \text{ N/m}^{3/2}$ , represent respectively soft and hard mallets. When using soft mallets, the sounds produced are smooth, as most of the energy is excited at lower frequencies. Conversely, the much brighter sounds excited by hard mallets are attested by the significant excitation of the higher frequency modes.

### 5.4 Bar material

Figure 10 also shows how significant the bar material is, for the instrument timbre. Here, the last two time-plots and spectrograms display the responses of a typical marimba bar, with the same fundamental frequency. Obviously, wood has a lower density than aluminium (about one third). However, the main effect of the material is, without doubt, the much higher

dissipation of wooden bars. Here, we recall that modal damping values of  $\zeta_m = 0.02\%$  and  $\zeta_m = 0.5\%$  were used (for all modes), respectively in the case of aluminium and wood bars. The consequences of this simple parameter change, when the subjective timbral qualities are concerned, go much beyond the mere decrease in response duration shown in Figure 10. Indeed, simulations using the lower damping value sound as impacted metal, while those using the higher damping value sound as impacted wood.

### 5.5 Bar shape: conventional designs

Figure 11 shows the time-responses and corresponding spectrograms of several “conventional” bars, with frequency ratios that might be found in xylophones, marimbas and vibraphones. Common variations include the second partial, at either 1:3 (one octave + one fifth) or 1:4 (two octaves), as well as the third partial, at either 1:9 (three octaves + one minor third) or 1:10 (three octaves + one major third). All these cases are illustrated in the figure, based in the optimized shapes obtained as shown in Sections 2 and 3. The

corresponding sounds show that influence of the second partial frequency is very easily perceived. However, for the untrained ear, the influence of the third partial is more subtle.

### 5.6 Bar shape: non-orthodox designs

We conclude by illustrating in Figure 12 the time-responses and corresponding spectrograms of the four unconventional bars optimized in Section 3. Here, one should bear in mind that the perceived sounds depend, not only on the tuned modes, but also on other higher frequency modes which are outside the optimized frequency range (and therefore “uncontrolled”). Here, we chose the modal relationships of  $1:2:3$ ,  $1:3:6:12$ ,  $1:2:4:8:16$  and  $1:5:10:15$ , not on the ground of their particular “musical” qualities, but only because such modal tunings lead to very different bar geometries, as well as response spectra. And, indeed, the sounds obtained are different, as can be inferred from the spectrograms in Figure 12.

The case  $1:2:3$  deserves a short comment, because it led to a somewhat unexpected sound. Indeed, from such frequency combination, one might naively expect a “sweet” sound, but what we obtained sounds harsh, almost as sounds issued from some gamelan instruments, for instance. What happens here is that the non-optimized forth and upper partials present frequencies which are relatively low. These are significantly excited and severely inharmonic. If we assume that such effect is undesirable, there is a lesson to extract from this example: Sometimes, one should design the optimization procedure not only on the basis of what is wanted, but also on the basis what is *not* wanted. This can be achieved easily: In the first case, penalty terms in the error-function should tax divergence between the computed modal frequencies and the target set. In the second case, penalties should tax proximity of the computed modal frequencies to any undesirable frequency range. Both aspects

can be easily combined in the optimization procedure.

## 6. Conclusion

Two important aspects of the design of percussion instruments have been addressed in this paper: (1) Geometry optimization of the vibrating component, and (2) Sound synthesis through nonlinear physical modelling. The feasibility of these two complementary approaches has been demonstrated.

Beyond enabling a systematic and cost-effective way of improving conventional instrument designs, an obvious advantage of optimization approaches is the possibility of developing non-conventional instruments with new sound qualities. We illustrated the various aspects discussed by optimizing and dynamically simulating several vibraphone and marimba bars. Bar/resonator vibro-acoustic coupling and radiation effects have not been yet incorporated in our computational model. Even so, the subjective quality of the simulated sounds was found quite satisfactory.

We intend to extend the present work in several directions. Concerning optimization, these include:

- optimization of resonator geometries, to control other acoustic modes beyond the first, in connection with the bar vibratory modes;
- optimization with respect to other aspects beyond modal frequencies, for instance the system modeshapes, in order to better control the radiated spectra;
- optimization of more complex problems, ranging from soundboard geometries (and bridge placement) to the design of optimized carillon bells;

Turning towards dynamical simulations, the most urgent aspects to include in our approach are the bar/resonator vibro-acoustic coupling and radiation. Some of these aspects are currently being addressed.

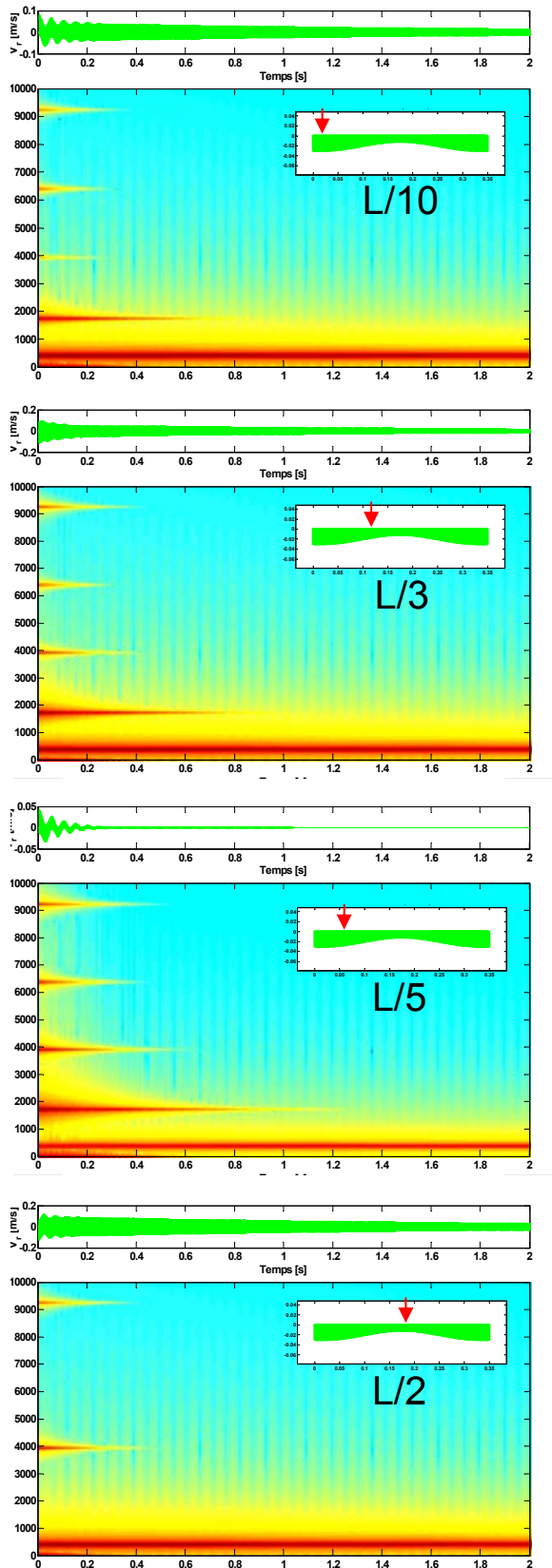


Figure 9: Vibratory responses of a 1:4:9 vibraphone bar as a function of the impact location  $x_c$  (contact stiffness  $K_c = 10^8 \text{ N/m}^{3/2}$ ).

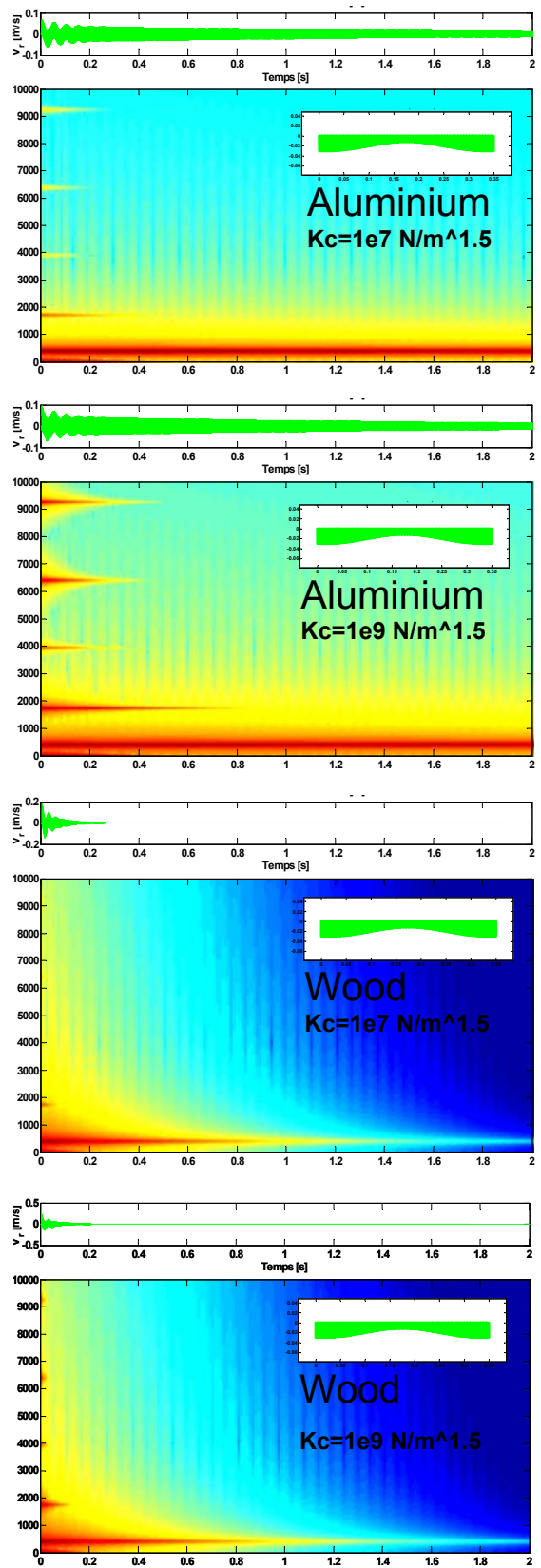


Figure 10: Vibratory responses of a 1:4:9 vibraphone bar as a function of the contact stiffness  $K_c$  and also of the bar material (impact location  $x_c = L/10$ ).

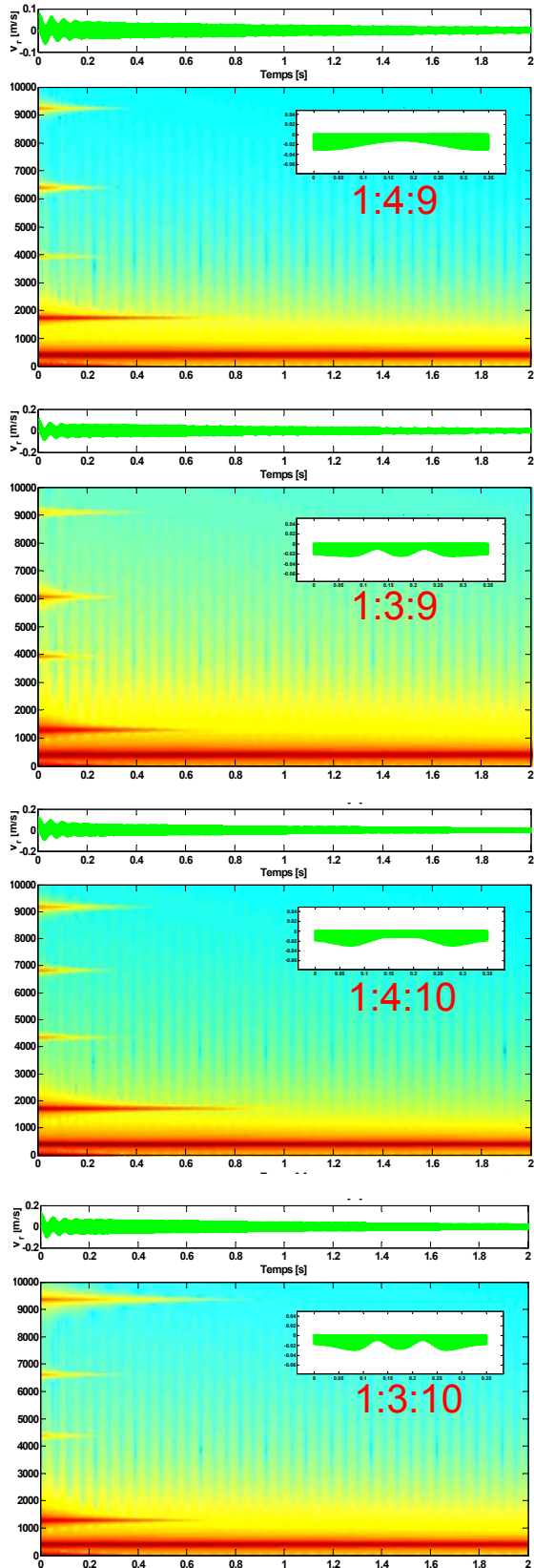


Figure 11: Vibratory responses of four near-conventional vibraphone bars (contact stiffness  $K_c = 10^8 \text{ N/m}^{3/2}$ , impact location  $x_c = L/10$ ).

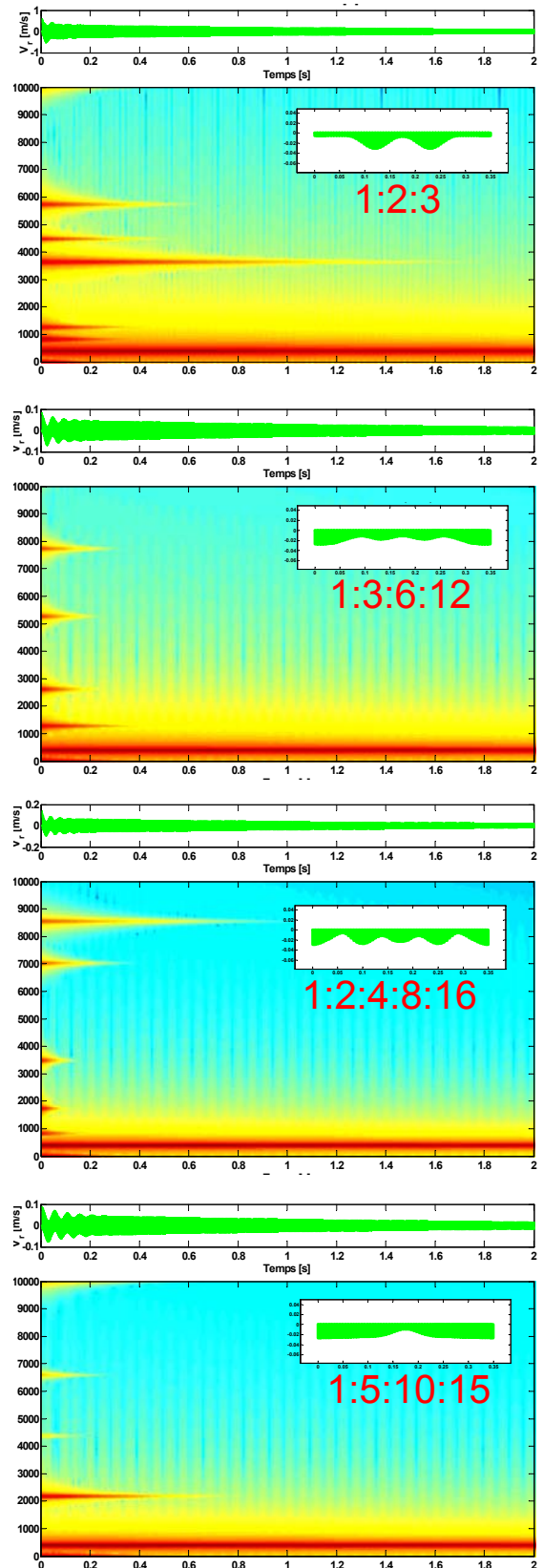


Figure 12: Vibratory responses of four non-orthodox vibraphone bars (contact stiffness  $K_c = 10^8 \text{ N/m}^{3/2}$ , impact location  $x_c = L/10$ ).

## Acknowledgement

Useful discussions with **Octávio Inácio** (Intituto Politécnico do Porto, IPP/ESMAE, Portugal) and his valuable assistance while performing preliminary experiments, are gladly acknowledged.

## References

- [1] W. H. Press, B. P. Flannery, S. A. Teukolky, W. T. Vettering: Numerical recipes: The art of scientific computing. Cambridge University Press, Cambridge (1989).
- [2] P. Venkataraman, Applied optimization with Matlab programming. John Wiley & Sons, New York (2002).
- [3] I. E. Grossmann (Ed.): Global optimization in engineering design. Kluwer Academic Publishers, Dordrecht (1996).
- [4] J. D. Pinter: Global optimization in action. Kluwer Academic Publishers, London (1996).
- [5] A. Schoofs, F. Asperen, P. Maas, A. Lehr: A carrillon of major-third bells: Computation of bell profiles using structural optimization. *Music Perception*, **4** (1987), 245-254.
- [6] F. Orduña-Bustamonte: Nonuniform beams with harmonically related overtones for use in percussion instruments. *Journal of the Acoustical Society of America*, **90** (1991), 2935-2941.
- [7] J. Petrolito, K. A. Legge: Optimal undercuts for the tuning of percussive beams. *Journal of the Acoustical Society of America*, **102** (1997), 2432-2437.
- [8] W. Kausel, P. Anglmayer, G. Widholm: A computer program for optimization of brass instruments: Part 1 - Concept, implementation. *Forum Acusticum 1999, Joint 137th Meeting of the Acoustical Society of America and 2nd Meeting of the European Acoustics Association*, Berlin, 15-19 March 1999.
- [9] P. Anglmayer, W. Kausel, G. Widholm: A computer program for optimization of brass instruments: Part 2 - Applications, practical examples. *Forum Acusticum 1999, Joint 137th Meeting of the Acoustical Society of America and 2nd Meeting of the European Acoustics Association*, Berlin, 15-19 March 1999.
- [10] L. Henrique, J. Antunes, J. S. Carvalho: Design of musical instruments using global optimization techniques. *International Symposium of Musical Acoustics (ISMA 2001)*, Perugia, 10-14 September 2001.
- [11] L. Henrique, J. Antunes: Conception optimale des instruments à percussion: Stratégies d'optimisation géométrique. *6<sup>e</sup> Congrès Français d'Acoustique (CFA 2002)*, Lille, 8-11 April 2002.
- [12] M. Tinnsten, P. Carlsson: Numerical optimization of geometrical dimensions and determination of material parameters for violin tops. *Forum Acusticum 2002*, Sevilla, 16-20 September 2002.
- [13] L. Henrique, J. Antunes, J. S. Carvalho: Shape optimization techniques for musical instrument design. *144<sup>th</sup> Meeting of the Acoustical Society of America*, Cancun, 2-6 December 2002.
- [14] I. Bork: Practical tuning of xilophone bars and resonators. *Applied Acoustics*, **46** (1995), 103-127.
- [15] P. Van Laarhoven, E. Aarts: Simulated annealing: Theory and applications. Kluwer Academic Publishers, Dordrecht (1987).
- [16] M. E. McIntyre, R. T. Shumacher, J. Woodhouse: On the oscillations of musical instruments. *Journal of the Acoustical Society of America*, **74** (1983), 1325-1345.
- [17] A. Chaigne: Some thoughts on physical modeling. *Proceedings of SMAC 93*, Royal Swedish Academy of Music, Stockholm (1993).
- [18] A. Hirschberg, J. Kergomard, G. Weinreich: Mechanics of musical

- instruments. Springer-Verlag, Wien (1995).
- [19] T. D. Rossing: The science of percussion instruments. World Scientific, Singapore (2000).
- [20] A. Chaigne, V. Doutaut: Numerical simulation of xylophones: Part 1 – Time-domain modelling of the vibrating bars. *Journal of the Acoustical Society of America*, **101** (1997), 539-557.
- [21] V. Doutaut, D. Matignon, A. Chaigne: Numerical simulation of xylophones: Part 2 – Time-domain modelling of the resonator and of the radiated sound pressure. *Journal of the Acoustical Society of America*, **104** (1998), 1633-1647.
- [22] A. Chaigne, C. Lambourg: Time-domain simulation of damped impacted plates: Part 1 – Theory and experiments. *Journal of the Acoustical Society of America*, **109** (2001), 1422-1432.
- [23] C. Lambourg, A. Chaigne, D. Matignon: Time-domain simulation of damped impacted plates: Part 2 – Numerical model and results. *Journal of the Acoustical Society of America*, **109** (2001), 1433-1447.
- [24] C. Touzé, O. Thomas, A. Chaigne: Vibrations non-linéaires de plaques. *6<sup>e</sup> Congrès Français d'Acoustique (CFA 2002)*, Lille, 8-11 April 2002.
- [25] J. Antunes, L. Henrique: Conception optimale des instruments à percussion: Synthèse sonore par modèle physique. *6<sup>e</sup> Congrès Français d'Acoustique (CFA 2002)*, Lille, 8-11 April 2002.
- [26] O. Inácio, L. Henrique, J. Antunes: Simulation of the oscillation regimes of bowed bars: A nonlinear modal approach. *Proceedings of the ASME International Mechanical Engineering Congress (IMECE'02)*, New Orleans, 17-22 November 2002. Also in *Communications in Nonlinear Science and Numerical Simulation* (in print).
- [27] A. Akay, M. T. Bengisu, M. Latcha: Transient acoustic radiation from impacted beam-like structures. *Journal of Sound and Vibration*, **91** (1983), 135-145.
- [28] A. Frendi, L. Maestrello, A. Bayliss: Coupling between plate vibration and acoustic radiation. *Journal of Sound and Vibration*, **177** (1994), 207-226.
- [29] S. Schedin, C. Lambourg, A. Chaigne: Transient sound fields from impacted plates: Comparison between numerical simulations and experiments. *Journal of Sound and Vibration*, **221** (1999), 471-490.
- [30] C. Touzé, A. Chaigne: Lyapunov exponents from experimental time-series: Application to cymbal vibrations. *Acta Acustica*, **86** (2000), 557-567.
- [31] O. Thomas, C. Touzé, A. Chaigne: Nonlinear resonances in large-deflection vibrations of free-edge circular plates. *7<sup>th</sup> International Congress of Sound and Vibration*, Garmisch-Partenkirchen, 4-7 July 2002.
- [32] A. Chaigne, C. Touzé, O. Thomas: Nonlinear axisymmetric vibration of gongs. *International Symposium of Musical Acoustics (ISMA 2001)*, Perugia, 10-14 September 2001.
- [33] A. Chaigne, M. Fontaine, O. Thomas, C. Touzé: Vibrations of shallow spherical shells and gongs: A comparative study. *Forum Acousticum 2002*, Sevilla, 16-20 September 2002.
- [34] K. F. Graff: Wave motions in elastic solids. Dover Publications, New York (1975).
- [35] I. Bork, A. Chaigne, L.-C. Trebuchet, M. Kosfelder, D. Pillot: Comparison between modal analysis and finite element modelling of a marimba bar. *Acta Acustica*, **85** (1999), 258-266.
- [36] D. Holz: Acoustically important properties of xylophone-bar materials: Can tropical woods be replaced by European species? *Acta Acustica*, **82** (1996), 878-884.
- [37] H. W. Kuhn, A. W. Tucker: Nonlinear programming. *Proceedings of the 2<sup>nd</sup>*

- Berkeley Symposium on Mathematical Statistics and Probability*. University of California Press (1951).
- [38] J. S. Arora: Introduction to optimum design. McGraw-Hill, New York (1989).
- [39] N. Metropolis, A. Rosenbluth, M. Rosenbluth, A. Teller, E. Teller: Equations of state calculations by fast computing machines. *Journal of Chemical Physics*, **21** (1953), 1087-1092.
- [40] S. Kirkpatrick, G. C. Gelatt, M. P. Vecchi: Optimization by simulated annealing. *Science*, **220** (1983), 671-680.
- [41] D. Vanderbilt, S. G. Louie: A monte-carlo simulated annealing approach to optimization over continuous variables. *Journal of Computational Physics*, **56** (1984), 259-271.
- [42] P. van Laarhoven, E. Arts: Simulated annealing: Theory and applications. Reidel, Dordrecht (1987).
- [43] E. Arts, J. Korst: Simulated annealing and Boltzmann machines. Wiley Interscience, New York (1989).
- [44] C. Lambourg, A. Chaigne: Time-domain modelling of damping in plates. *133rd Meeting of the Acoustical Society of America*, Penn State, 16-20 June 1997.
- [45] T. Hélie, D. Matignon: Damping models for the sound synthesis of bar-like instruments. *Proceedings of the Seventh International Conference on Systemics, Cybernetics and Informatics (SCI-2001)*, Orlando, 22-25 July 2001.
- [46] I. Bork: Measuring the acoustical properties of mallets. *Applied Acoustics*, **30** (1990), 207-218.